Online supplement to "Covariability of dynamics and composition in the Asian monsoon tropopause layer from satellite observations and reanalysis products"

Shenglong Zhang[1,2], Jiao Chen[1], Jonathon S. Wright[1], Sean M. Davis[3], Jie Gao[4], Paul Konopka[5], Ninghui Li[1], Mengqian Lu[2], Susann Tegtmeier[6], Xiaolu Yan[7], Guang J. Zhang[8], and Nuanliang Zhu[9]

[1]Department of Earth System Science, Tsinghua University, Beijing, China
[2]Department of Civil and Environmental Engineering, The Hong Kong University of Science and Technology, Hong Kong, China
[3]Earth System Research Laboratory, National Oceanic and Atmospheric Administration, Boulder, Colorado, USA
[4]Laoshan Laboratory, Qingdao, China
[5]Forschungszentrum Jülich (IEK-7: Stratosphere), Jülich, Germany
[6]Department of Physics and Engineering Physics, University of Saskatchewan, Saskatoon, Canada
[7]Institute of Tibetan Plateau Meteorology, Chinese Academy of Meteorological Sciences, Beijing, China
[8]Scripps Institution of Oceanography, La Jolla, California, USA
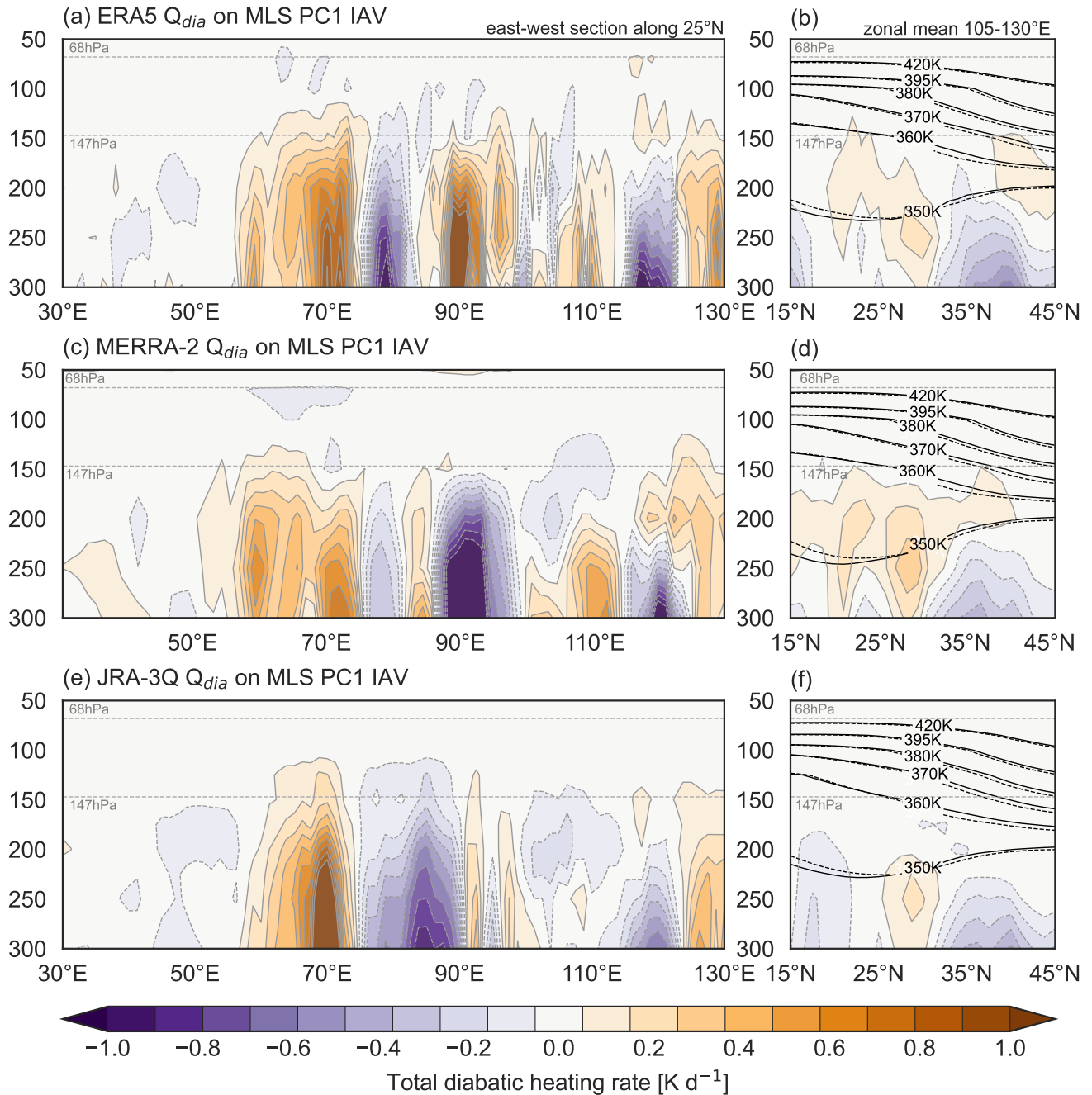[9]Department of the Geophysical Sciences, University of Chicago, Chicago, Illinois, USA

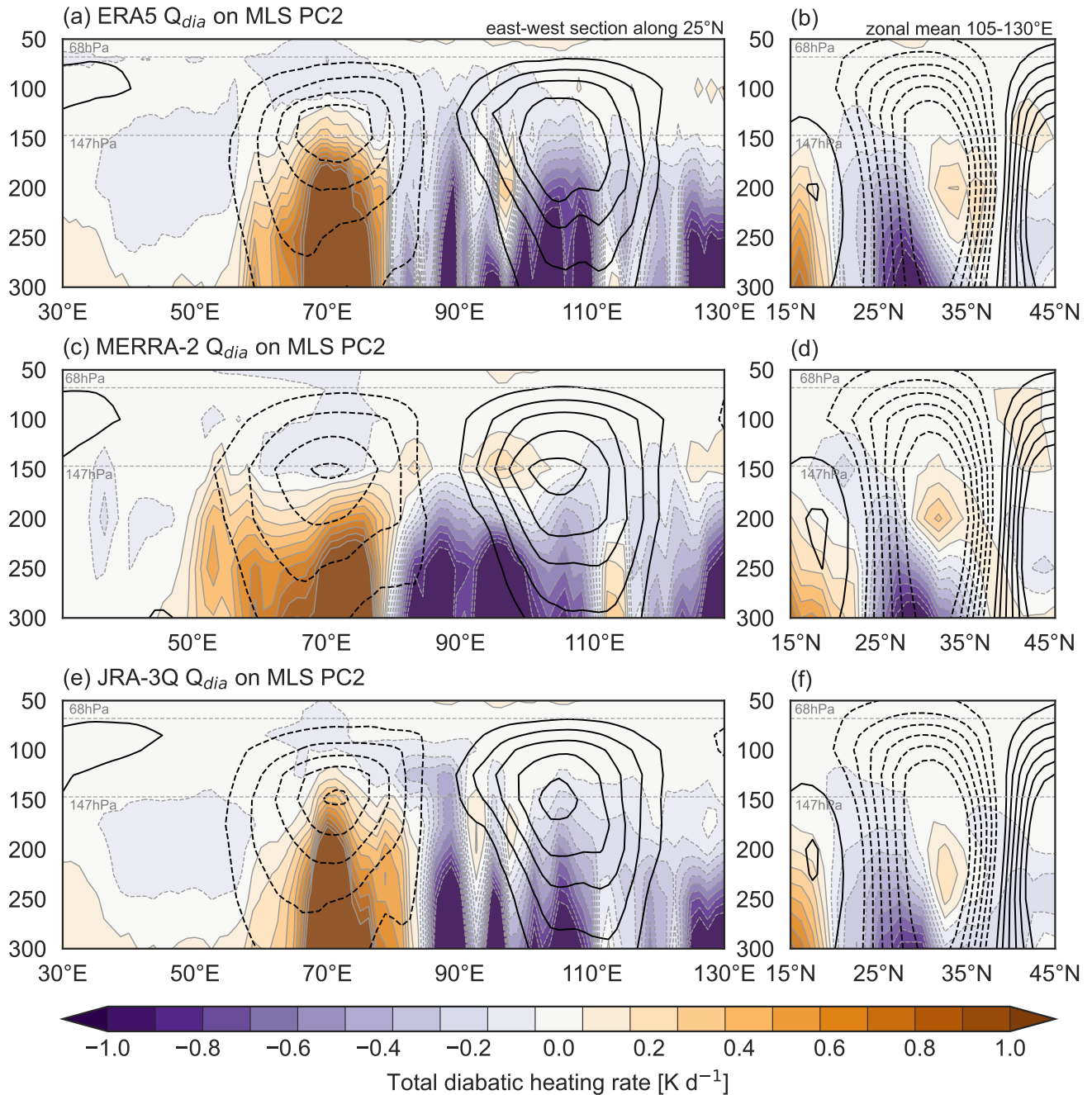**Correspondence:** Jonathon S. Wright (jswright@tsinghua.edu.cn)

Abstract. This online supplement contains 19 figures that support the reanalysis intercomparison component of this paper by extending evaluations presented in the main text to additional reanalysis products:

(1) **Figures S1–S3.** Total diabatic heating anomalies from ERA5, MERRA-2, and JRA-3Q regressed onto the first three principal components from Aura MLS (Figure 4 in the main text).

(2) **Figure S4.** Yearly variations in model internal dynamics, physics, and assimilation effects over the northwestern and northeastern quadrants (Figure 7 in the main text).

(3) **Figures S5–S7.** Water vapor, ozone, and dynamical and thermodynamic anomalies regressed onto the interannual variability of first principal component from Aura MLS for all reanalysis products (Figure 9 in the main text).

(4) **Figure S8.** CO anomalies regressed onto the first three principal components from Aura MLS (Figures 9d, 12d, and 13d in the main text).

(5) **Figure S9.** Direct lead–lag comparisons supporting the quadratic cycle of water vapor among the moist and dry phase of the second and third principal components (Figure 11 in the main text).

(6) **Figures S10–S16.** Water vapor, ozone, and dynamical and thermodynamic anomalies regressed onto the second and third principal components from Aura MLS for all reanalysis products (Figures 11–14 in the main text).

(9) **Figures S17–S19.** Anomalous water vapor tendencies for ERA5, JRA-3Q, and MERRA-2 composited for the moist and dry phases of the second and third principal components based on Aura MLS (Figure 15 in the main text).
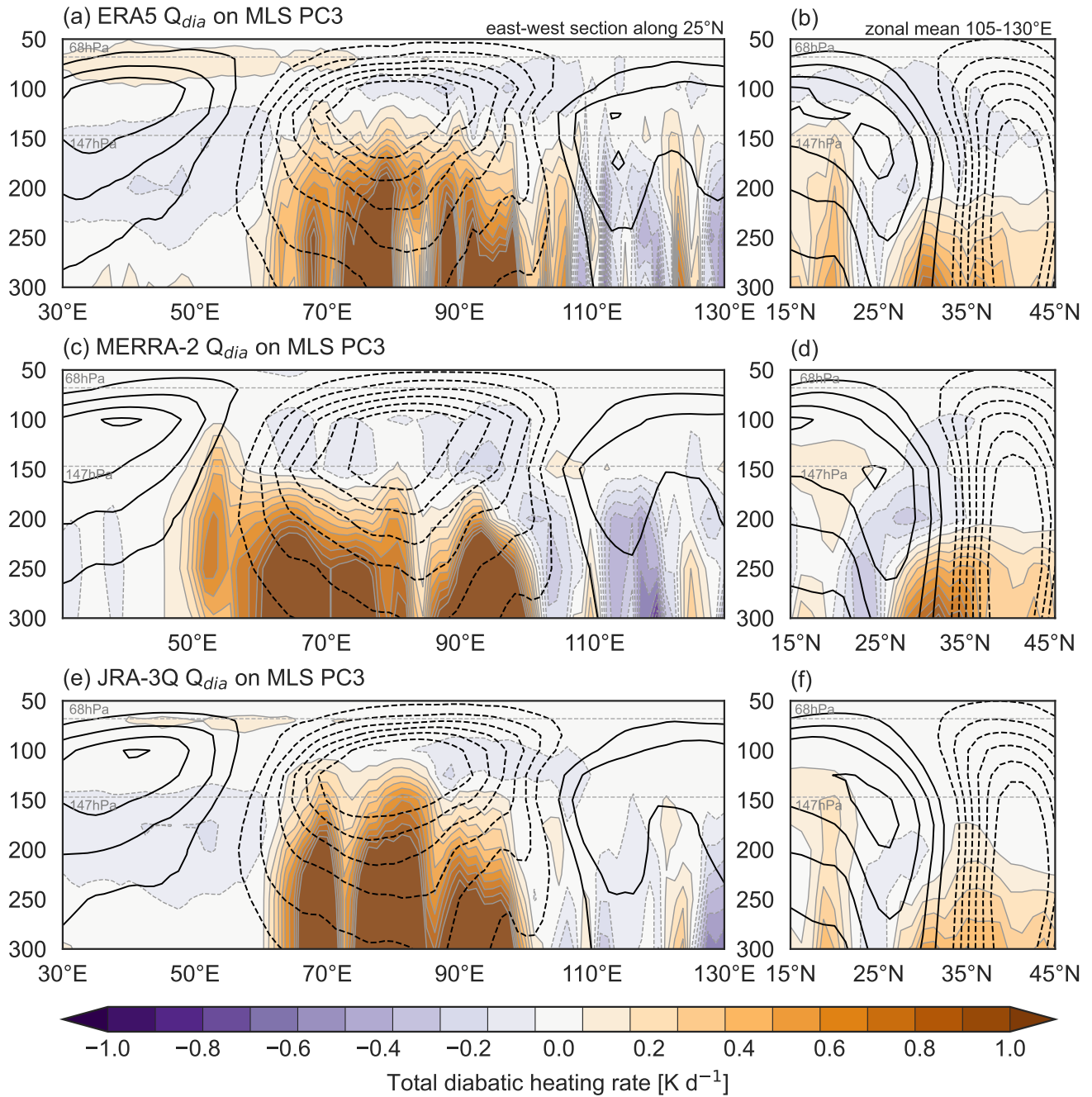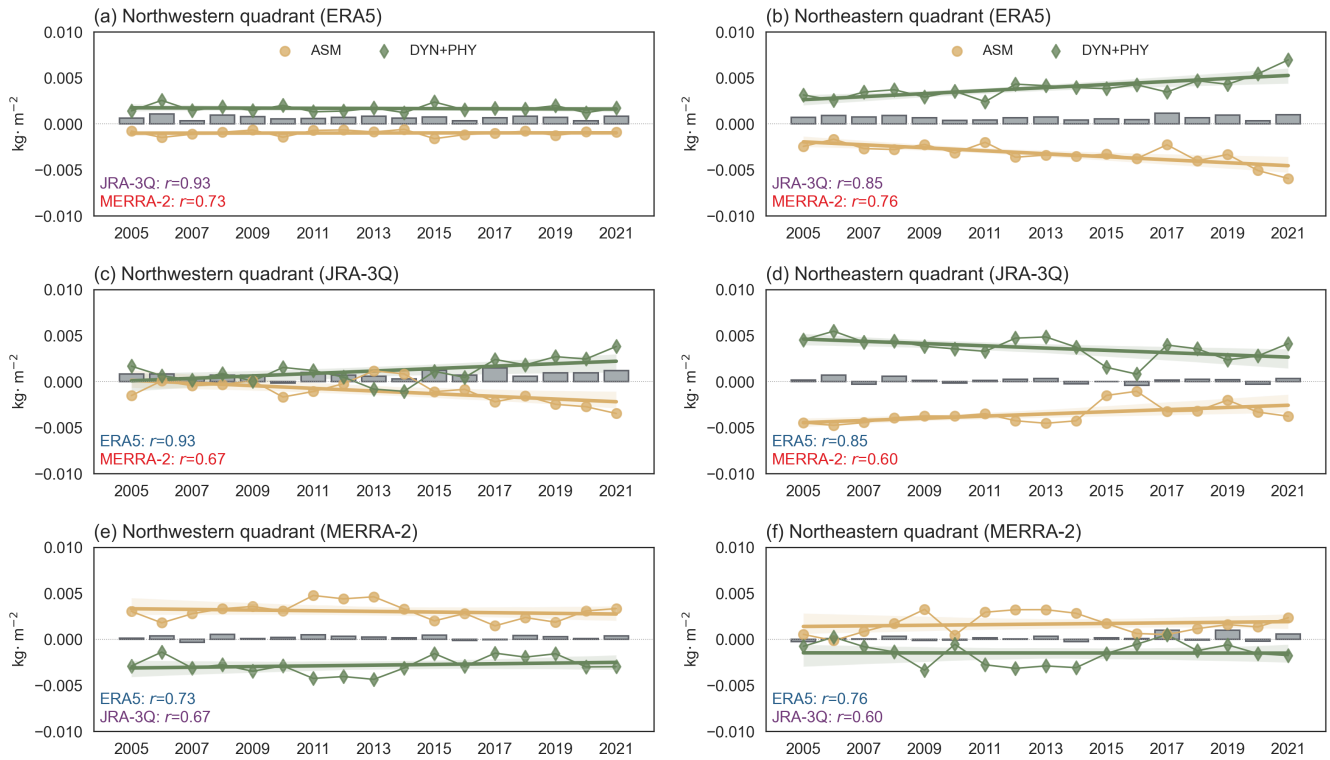
Figure S1. Composite diabatic heating anomalies based on (a)–(b) ERA5, (c)–(d) MERRA-2, (e)–(f) JRA-3Q conditioned on the interannual variability component of PC1 of LSWV variability from Aura MLS (Fig. 1c, Fig. 3c). Composite anomalies are calculated as the difference between averages over pentads with PC1 ≥ 1 and pentads with PC1 ≤ -1. Diabatic heating anomalies are evaluated (a,c,e) along 25°N and (b,d,f) zonally averaged over 105°E–130°E. Zonal mean isentropic surfaces (black contours in right column) are shown for both PC1 ≥ 1 (solid lines) and PC1 ≤ -1 (dotted lines). This figure shows results based on multiple reanalyses as context for Figure 4a in the main text.
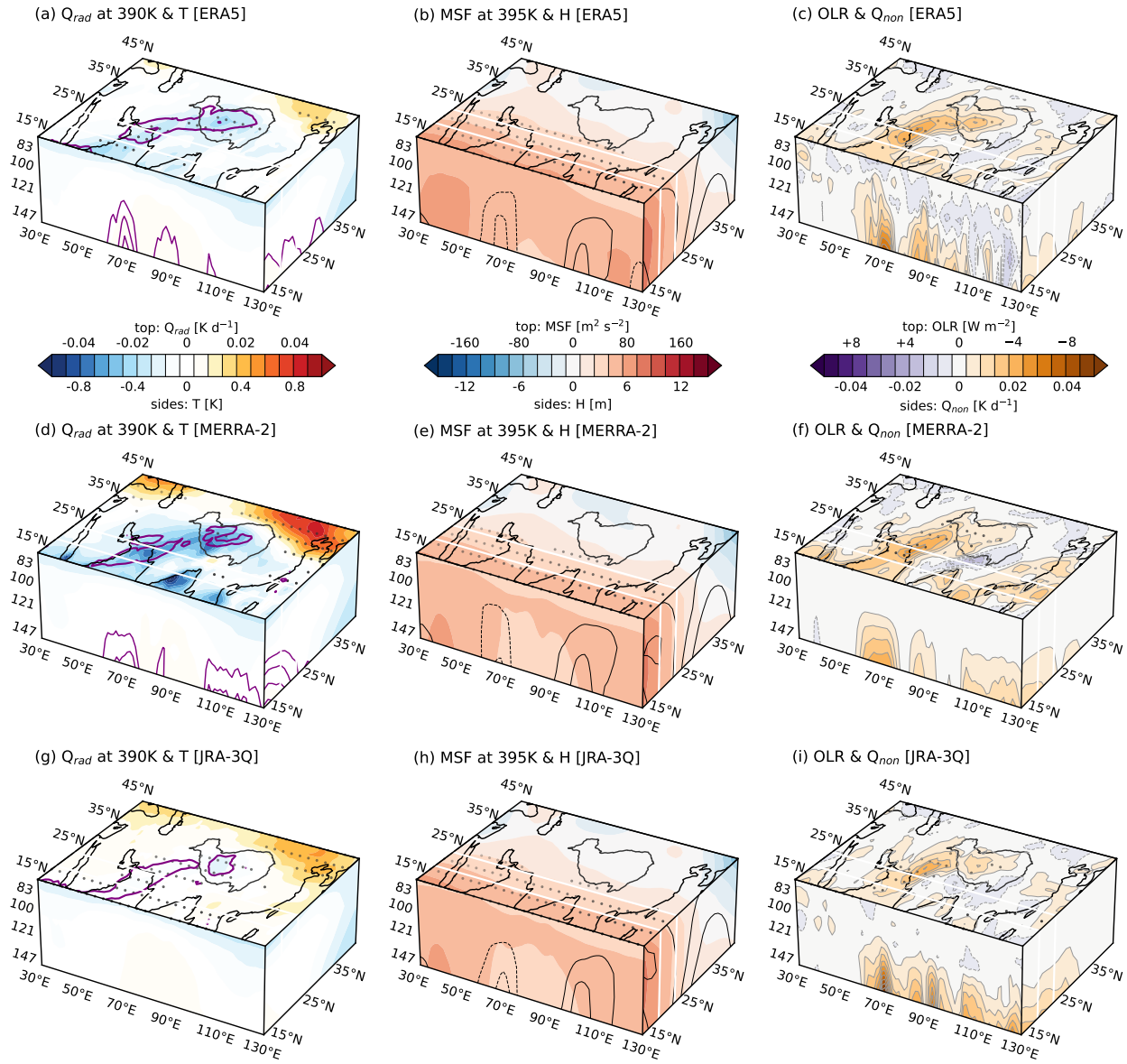
Figure S2. Composite diabatic heating anomalies based on (a)–(b) ERA5, (c)–(d) MERRA-2, (e)–(f) JRA-3Q conditioned on the second principal component (PC2) of LSWV variability from Aura MLS (Fig. 2a, Fig. 3d). Composite anomalies are calculated as the difference between averages over pentads with PC2 ≥ 1 and pentads with PC2 ≤ -1. Diabatic heating anomalies are evaluated (a,c,e) along 25°N and (b,d,f) zonally averaged over 105°E–130°E. Meridional (a,c,e) and zonal (b,d,f) wind anomalies (black contours) are shown at intervals of $1\,\mathrm{m\,s^{-1}}$ from $\pm 1\,\mathrm{m\,s^{-1}}$. This figure shows results based on multiple reanalyses as context for Figure 4b in the main text.
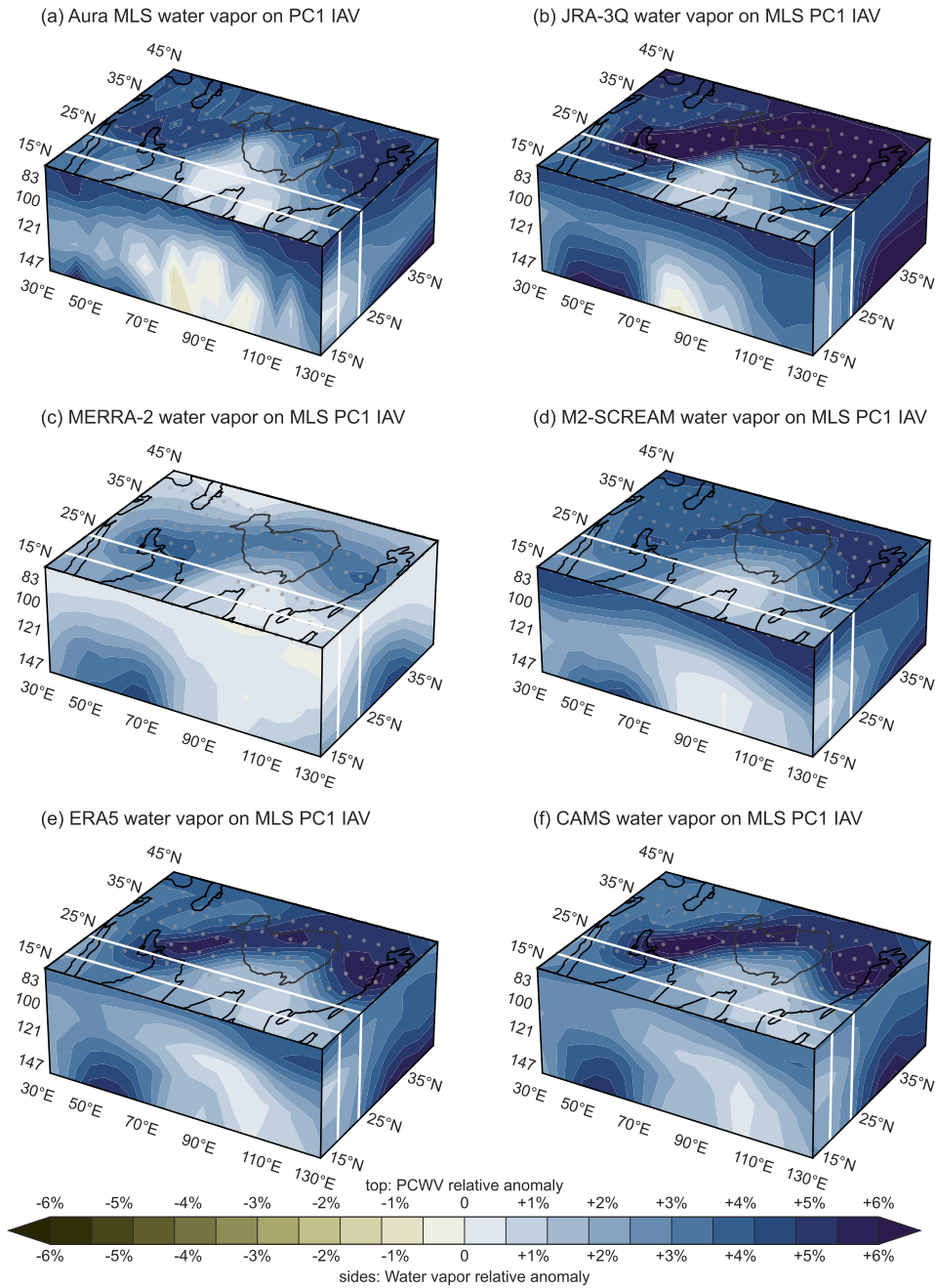
Figure S3. Composite diabatic heating anomalies based on (a)–(b) ERA5, (c)–(d) MERRA-2, (e)–(f) JRA-3Q conditioned on the third principal component (PC3) of LSWV variability from Aura MLS (Fig. 2b, Fig. 3e). Composite anomalies are calculated as the difference between averages over pentads with PC3 ≥ 1 and pentads with PC3 ≤ -1. Diabatic heating anomalies are evaluated (a,c,e) along 25°N and (b,d,f) zonally averaged over 105°E–130°E. Meridional (a,c,e) and zonal (b,d,f) wind anomalies (black contours) are shown at intervals of $1\,\mathrm{m\,s^{-1}}$ from $\pm 1\,\mathrm{m\,s^{-1}}$. This figure shows results based on multiple reanalyses as context for Figure 4c in the main text.
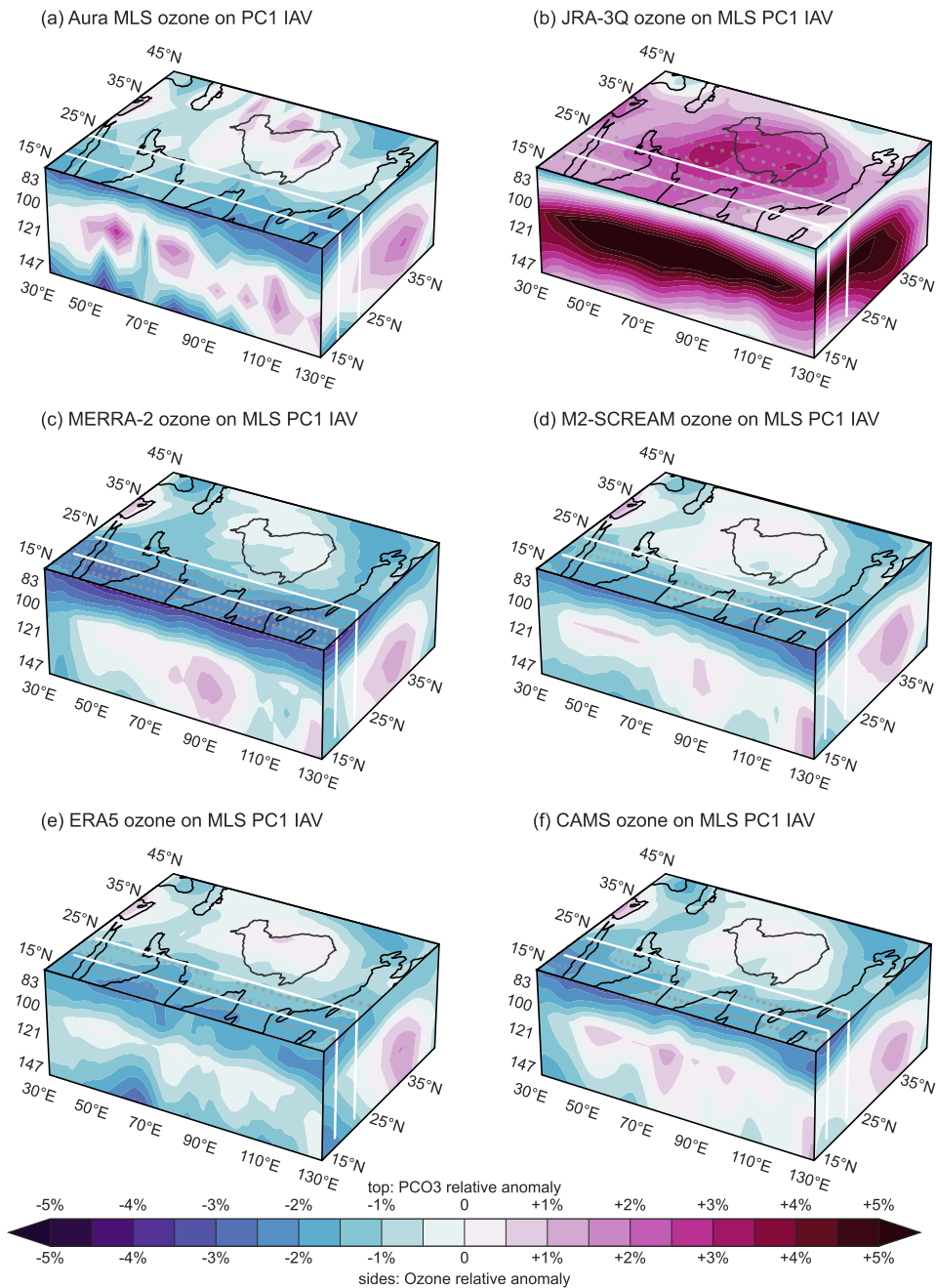
Figure S4. Yearly variations in the sum of the dynamics and physics terms (green lines), assimilation increments (yellow lines), and time rate of changes in partial column water vapor (gray boxes) in the monsoon tropopause layer based on (a,b) ERA5, (c,d) JRA-3Q, and (e,f) MERRA-2 over (a,c,e) the northwestern quadrant (25°N–45°N,30°E–90°E) and (b,d,f) the northeastern quadrant (25°N–45°N,90°E–130°E) of the monsoon anticyclone. Correlation coefficients between net water vapor tendency time series based on individual reanalyses are listed in the lower left corner of each panel.
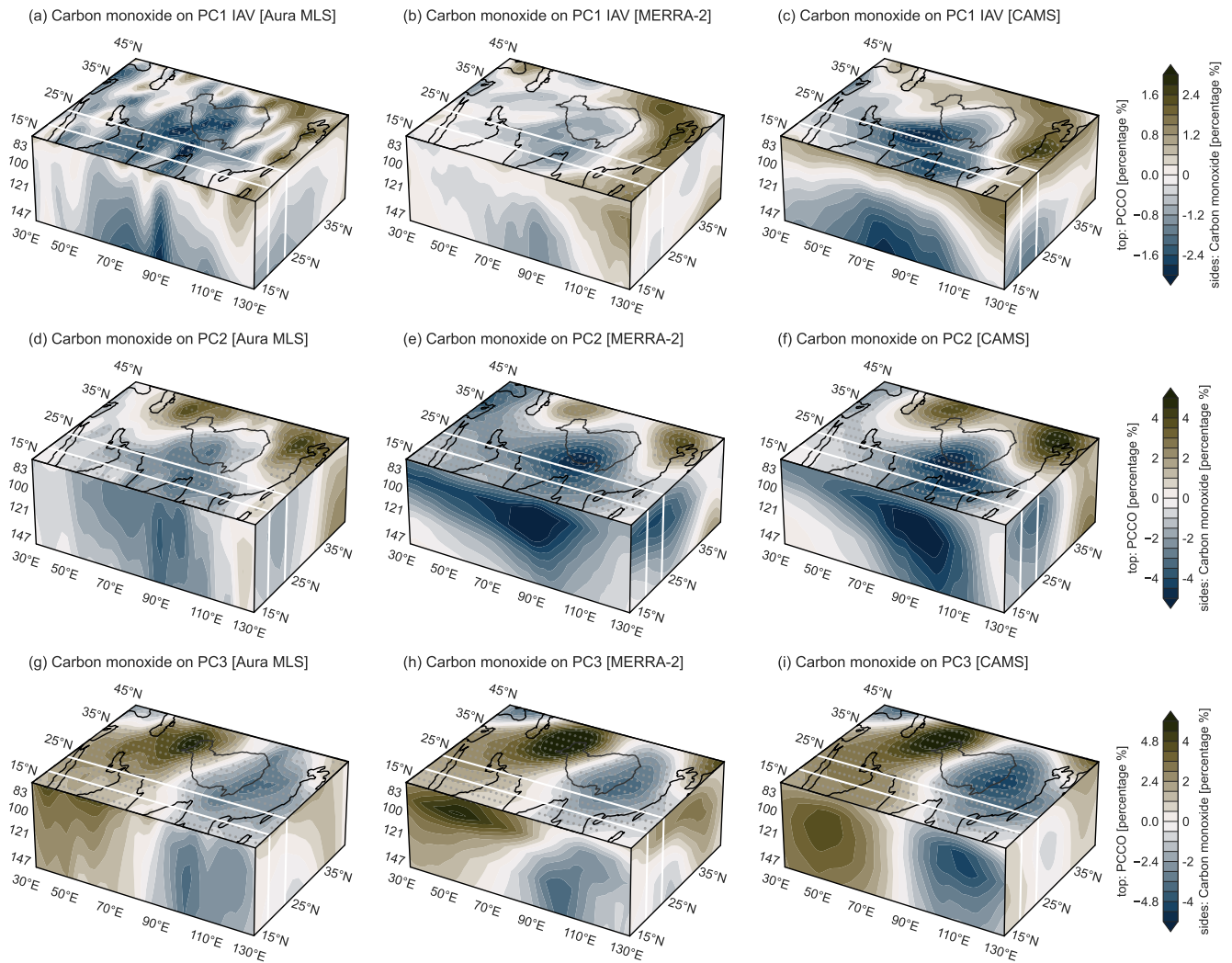
Figure S5. Deseasonalized anomalies regressed onto the interannual variability component of PC1 from Aura MLS in the monsoon tropopause layer (Fig. 3c): (a) radiative heating on the 390 K isentropic surface (shading) and high cloud cover (green contours; top face), and temperature (shading) and cloud ice water content (purple contours; side faces) based on ERA5; (b) Montgomery streamfunction on the 395 K isentropic surface (top face) and geopotential height (shading; side faces) based on ERA5; (c) outgoing longwave radiation (top face; sign reversed) and non-radiative heating (side faces) based on ERA5. (d,e,f) As in (a,b,c) but for MERRA-2. (g,h,i) As in (a,b,c) but for JRA-3Q. Black contours in (b,e,h) indicate anomalies in the meridional (south face) and zonal (east face) wind. The location of the Tibetan Plateau is marked by a dark grey contour and the boundaries of the east–west transect are marked by white lines in all panels. Stippling on the top face indicates locations where regressions are significant at the 95% confidence level.
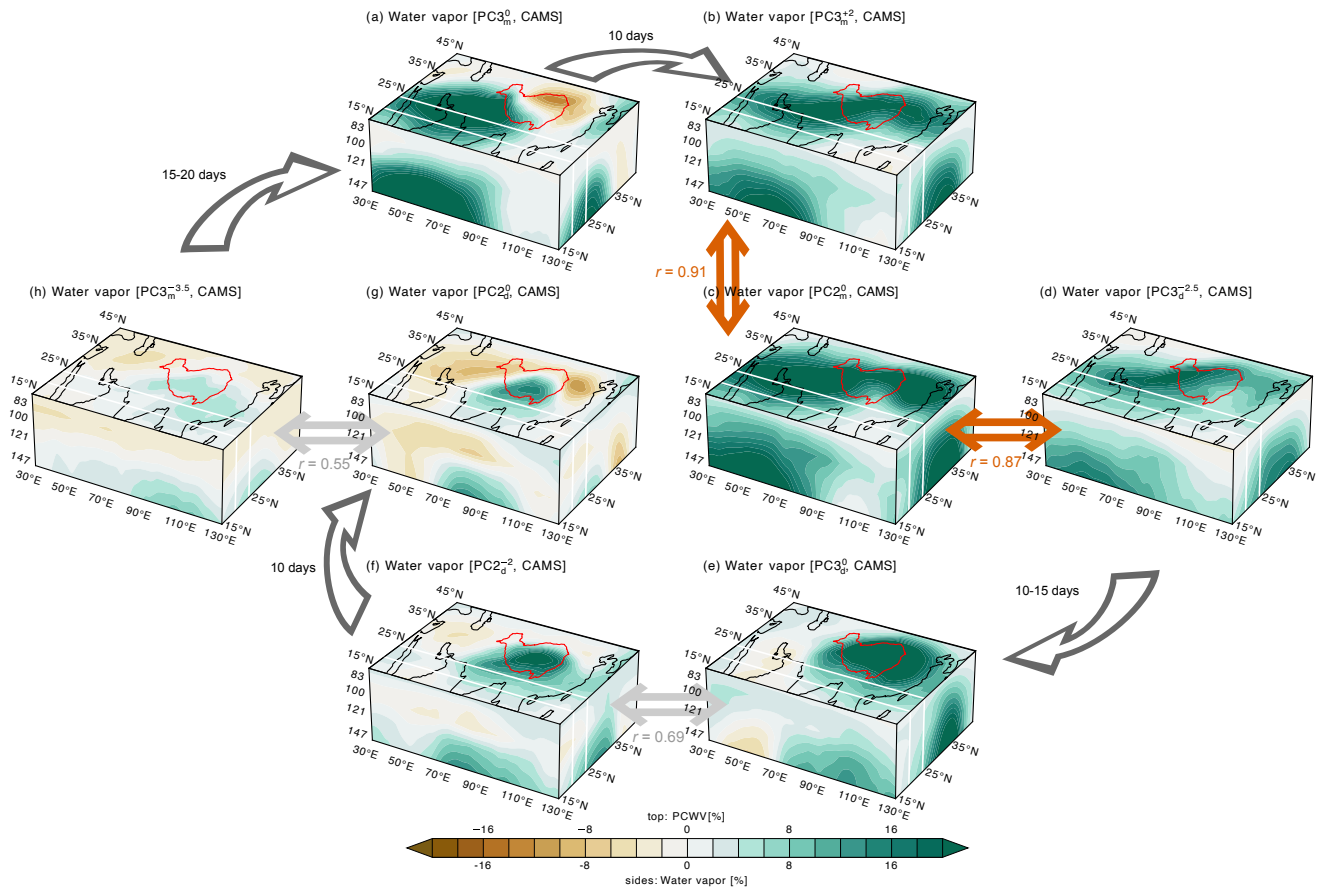
Figure S6. Vertical and horizontal structure of fractional changes in deseasonalized water vapor anomalies regressed onto the interannual variability component of PC1 from Aura MLS (Fig. 3c) based on (a) Aura MLS, (b) JRA-3Q, (c) MERRA-2, (d) M2-SCREAM, (e) ERA5, and (f) CAMS. Fractional anomalies in PCWV are shown on the top face, meridional mean water vapor within 20–25°N along the south face, and zonal mean water vapor within 30–130°E along the east face. The location of the Tibetan Plateau is marked by a dark grey contour and the boundaries of the east–west transect are marked by white lines in all panels. Stippling indicates where PCWV regressions are significant at the 95% confidence level. The figure corresponds to Figure 9c in the main text.
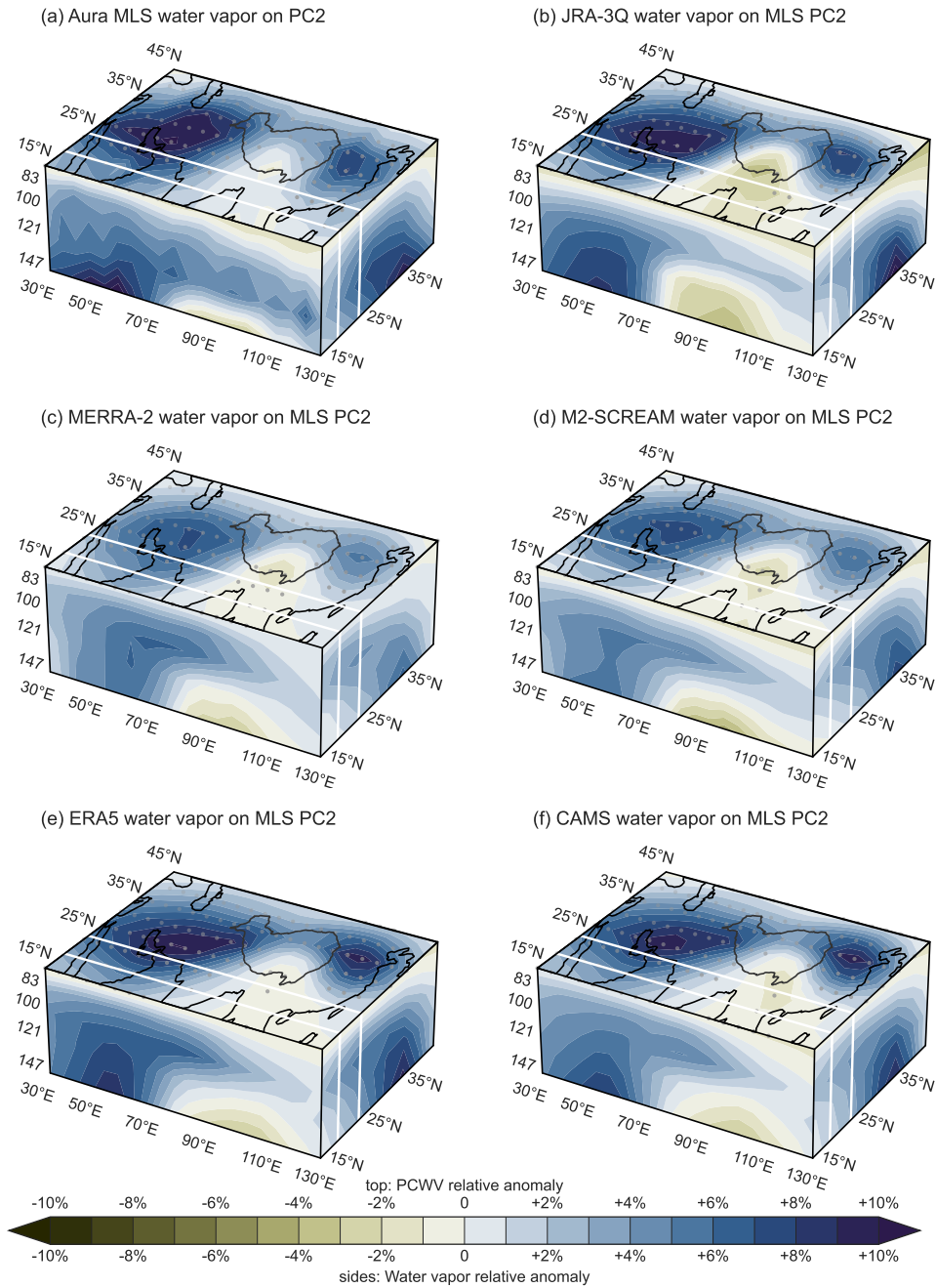
Figure S7. Vertical and horizontal structure of fractional changes in deseasonalized ozone anomalies regressed onto the interannual variability component of PC1 from Aura MLS (Fig. 3c) based on (a) Aura MLS, (b) JRA-3Q, (c) MERRA-2, (d) M2-SCREAM, (e) ERA5, and (f) CAMS. Fractional anomalies in PCO3 are shown on the top face, meridional mean ozone within 20–25°N along the south face, and zonal mean ozone within 30–130°E along the east face. The location of the Tibetan Plateau is marked by a dark grey contour and the boundaries of the east–west transect are marked by white lines in all panels. Stippling indicates where PCO3 regressions are significant at the 95% confidence level.
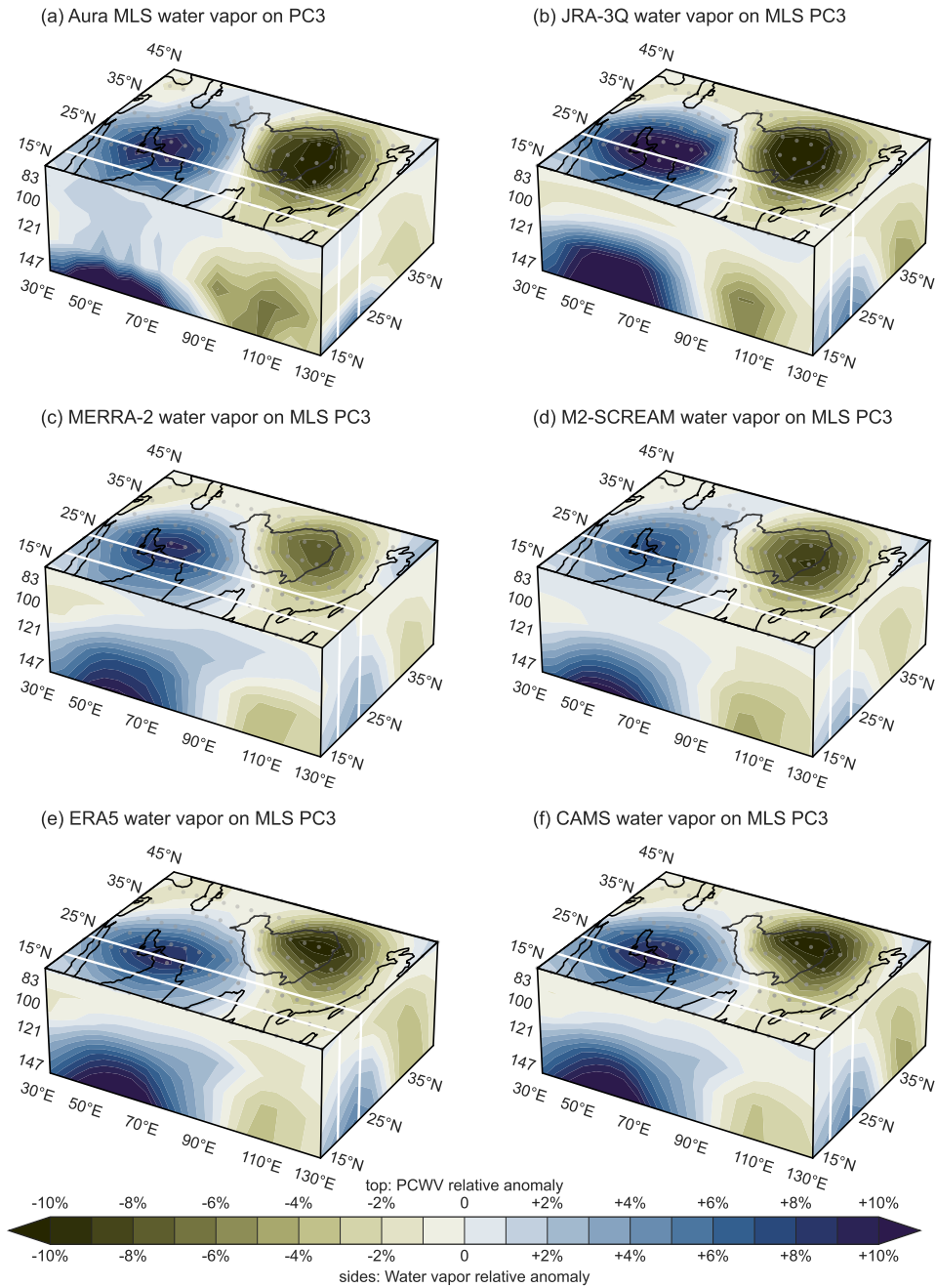
Figure S8. Vertical and horizontal structure of fractional changes in deseasonalized carbon monoxide (CO) anomalies regressed onto the interannual variability component of PC1 from Aura MLS (Fig. 3c) based on (a) Aura MLS, (b) MERRA-2, and (c) CAMS; PC2 of water vapor variability from Aura MLS (Fig. 3d) based on (d) Aura MLS, (e) MERRA-2, and (f) CAMS; and PC3 of water vapor variability from Aura MLS (Fig. 3e) based on (g) Aura MLS, (h) MERRA-2, and (i) CAMS. Fractional anomalies in PCCO are shown on the top faces, meridional mean ozone within 20–25°N along the south faces, and zonal mean ozone within 30–130°E along the east faces. The location of the Tibetan Plateau is marked by a dark grey contour and the boundaries of the east–west transect are marked by white lines in all panels. Stippling indicates where PCCO regressions are significant at the 95% confidence level. The figure corresponds to Figures 9d, 12d, and 13d in the main text.
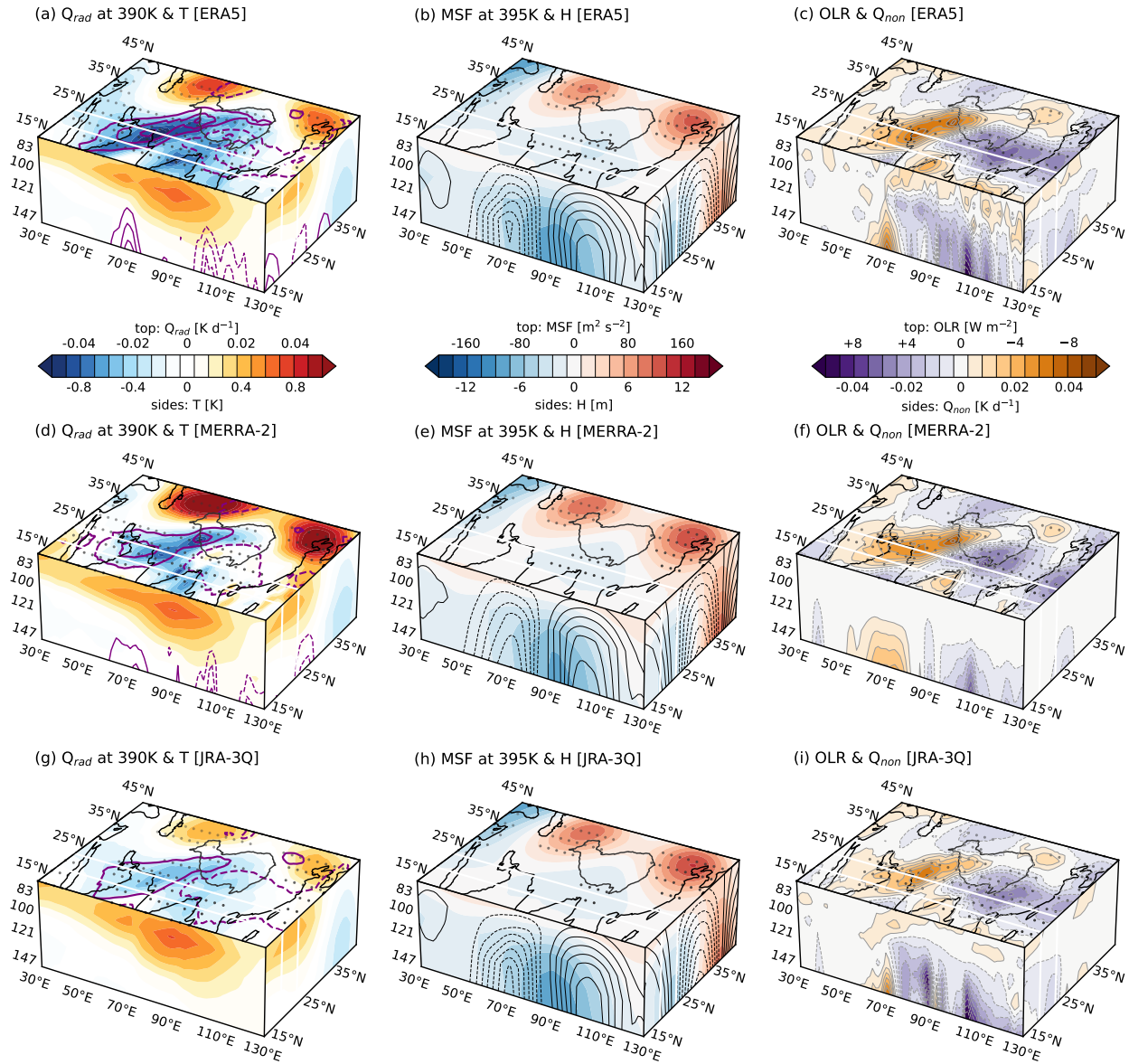
Figure S9. Distributions of tropopause layer water vapor anomalies illustrating the quadratic cycle of water vapor sub-seasonal variability based on CAMS. Water vapor relative anomalies are composited for the (a) principal component (PC3) moist phase, (b) two pentads after the PC3 moist phase, (c) the PC2 moist phase, (d) 2.5 pentads before the PC3 dry phase, (e) the PC3 dry phase, (f) two pentads before the PC2 dry phase, (g) the PC2 dry phase, and (h) 3.5 pentads before the PC3 moist phase. Area-weighted pattern correlations in PCWV between matched distributions are noted next to each set of double arrows. Curved arrows indicate transitions. The location of the Tibetan Plateau is marked by a red contour and the boundaries of the east–west transect are marked by white lines in all panels.
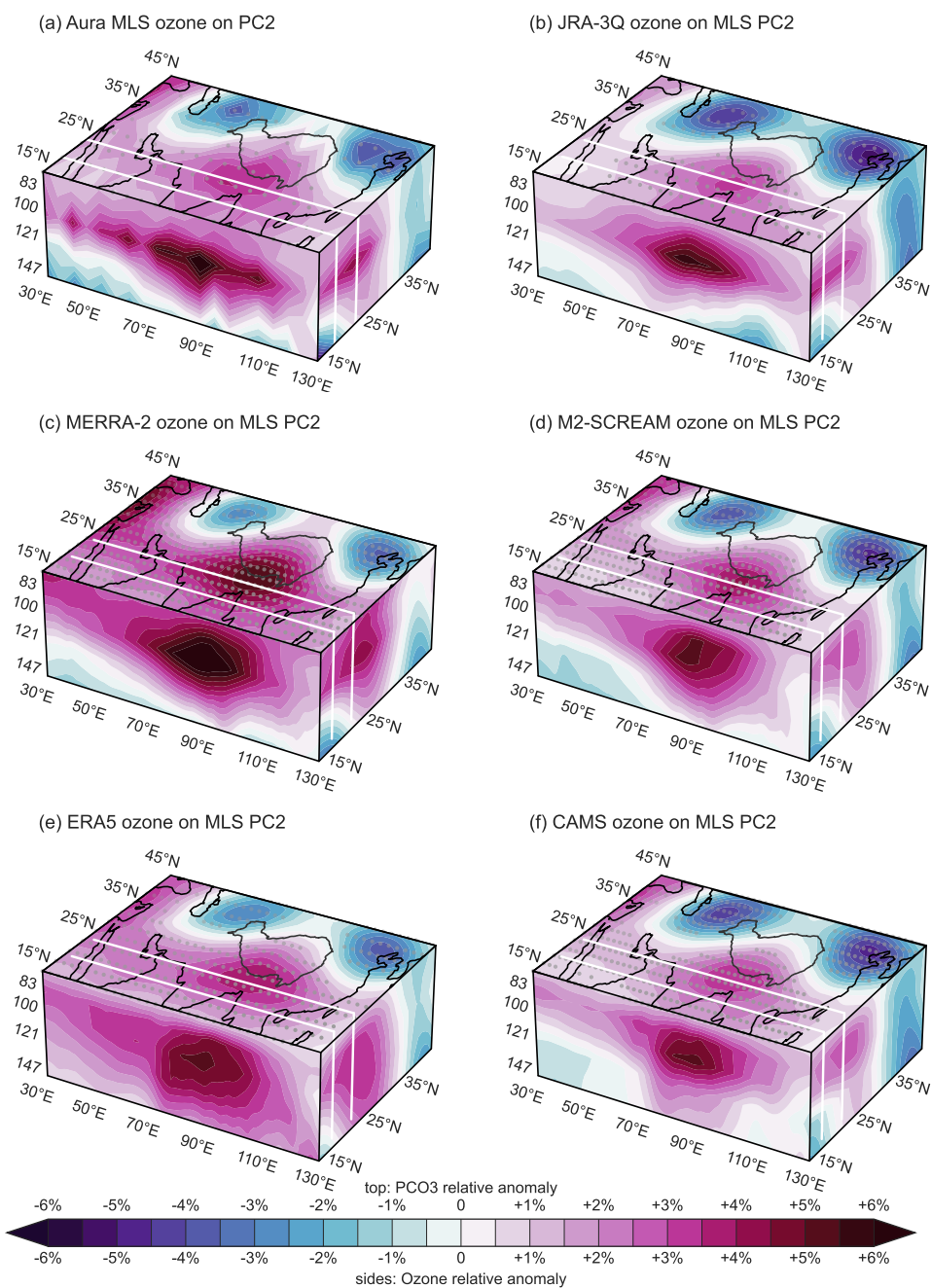
Figure S10. Vertical and horizontal structure of fractional changes in deseasonalized water vapor anomalies regressed onto PC2 from Aura MLS (Fig. 3d) based on (a) Aura MLS, (b) JRA-3Q, (c) MERRA-2, (d) M2-SCREAM, (e) ERA5, and (f) CAMS. Fractional anomalies in PCWV are shown on the top face, meridional mean water vapor within 20–25°N along the south face, and zonal mean water vapor within 30–130°E along the east face. The location of the Tibetan Plateau is marked by a dark grey contour and the boundaries of the east–west transect are marked by white lines in all panels. Stippling indicates where PCWV regressions are significant at the 95% confidence level. The figure corresponds to Figure 11b in the main text.
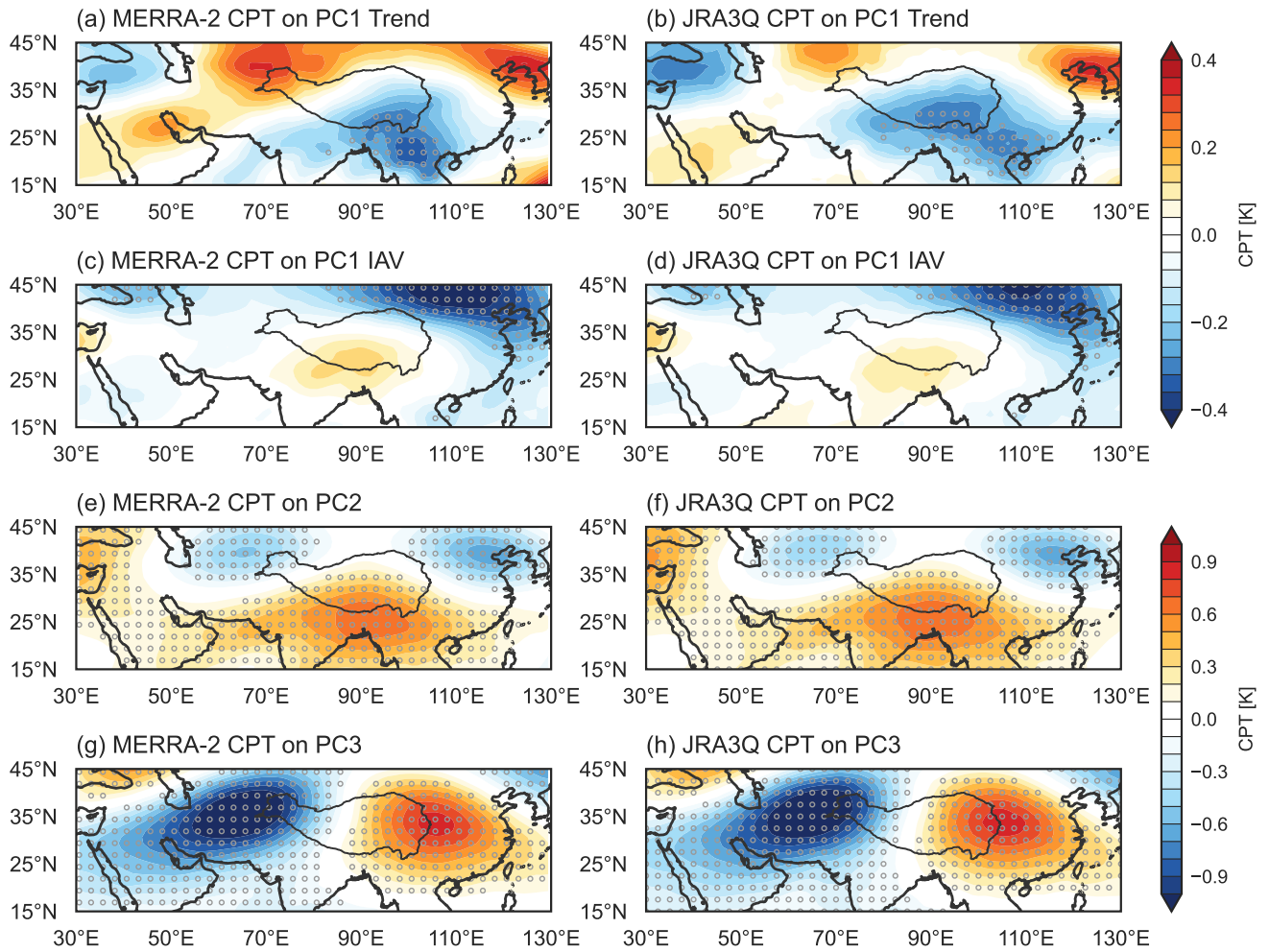
Figure S11. Vertical and horizontal structure of fractional changes in deseasonalized water vapor anomalies regressed onto PC3 from Aura MLS (Fig. 3e) based on (a) Aura MLS, (b) JRA-3Q, (c) MERRA-2, (d) M2-SCREAM, (e) ERA5, and (f) CAMS. Fractional anomalies in PCWV are shown on the top face, meridional mean water vapor within 20–25°N along the south face, and zonal mean water vapor within 30–130°E along the east face. The location of the Tibetan Plateau is marked by a dark grey contour and the boundaries of the east–west transect are marked by white lines in all panels. Stippling indicates where PCWV regressions are significant at the 95% confidence level. The figure corresponds to Figure 11a in the main text.
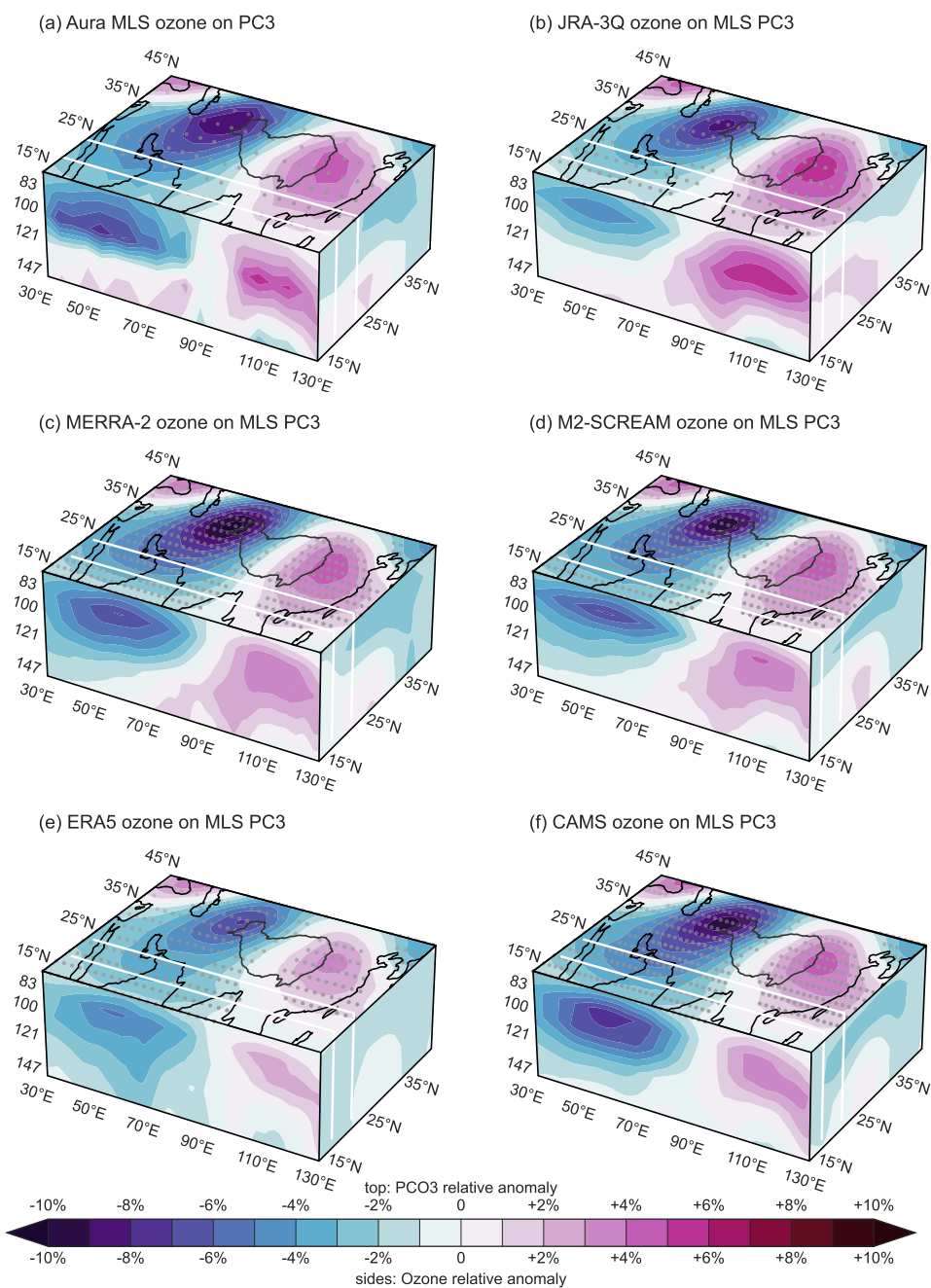
Figure S12. Deseasonalized anomalies regressed onto the second principal component (PC2) of water vapor variability in the monsoon tropopause layer based on Aura MLS (Fig. 3d): (a) radiative heating on the 390 K isentropic surface (shading) and high cloud cover (purple contours; top face), and temperature (shading) and cloud ice water content (purple contours; side faces) based on ERA5; (b) Montgomery streamfunction on the 395 K isentropic surface (top face) and geopotential height (shading; side faces) based on ERA5; (c) outgoing longwave radiation (top face; sign reversed) and non-radiative heating (side faces) based on ERA5. (d,e,f) As in (a,b,c) but for MERRA-2. (g,h,i) As in (a,b,c) but for JRA-3Q. Black contours in (b,e,h) indicate anomalies in the meridional (south face) and zonal (east face) wind. The location of the Tibetan Plateau is marked by a dark grey contour and the boundaries of the east–west transect are marked by white lines in all panels. Stippling on the top face indicates locations where regressions are significant at the 95% confidence level.
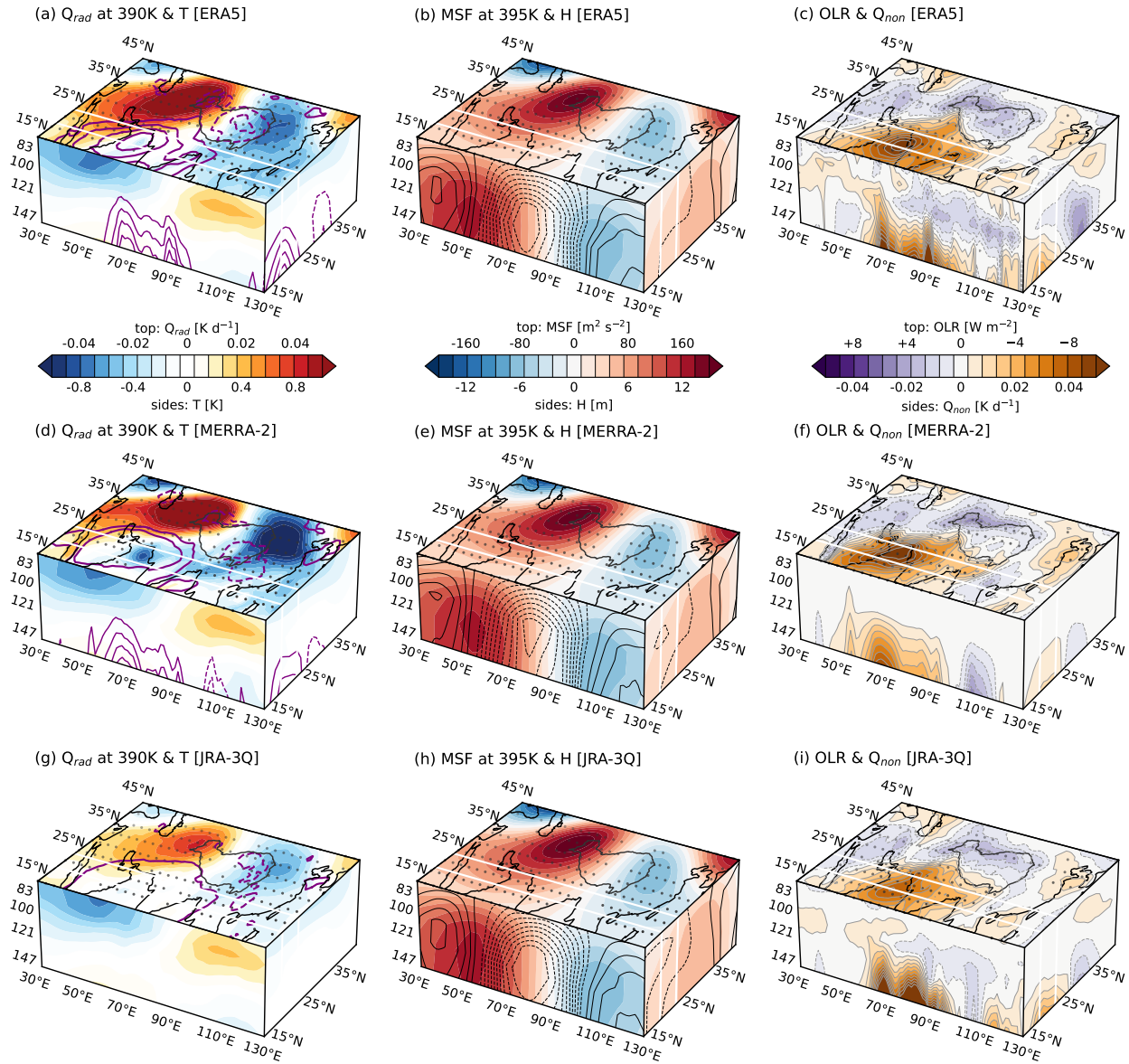
Figure S13. Vertical and horizontal structure of fractional changes in deseasonalized ozone anomalies regressed onto PC2 from Aura MLS (Fig. 3d) based on (a) Aura MLS, (b) JRA-3Q, (c) MERRA-2, (d) M2-SCREAM, (e) ERA5, and (f) CAMS. Fractional anomalies in PCO3 are shown on the top face, meridional mean ozone within 20–25°N along the south face, and zonal mean ozone within 30–130°E along the east face. The location of the Tibetan Plateau is marked by a dark grey contour and the boundaries of the east–west transect are marked by white lines in all panels. Stippling indicates where PCO3 regressions are significant at the 95% confidence level. The figure corresponds to Figure 13c in the main text.
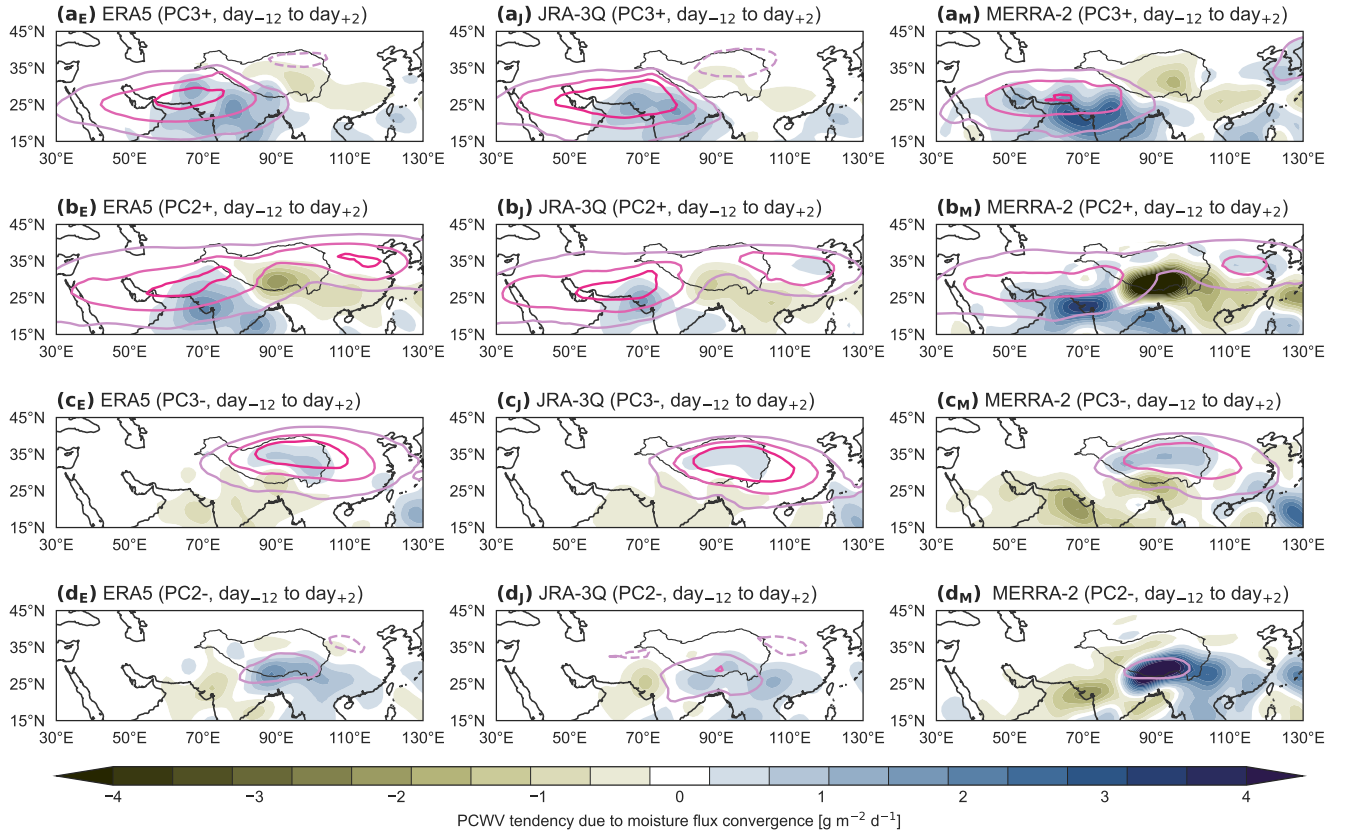
Figure S14. Deseasonalized anomalies of cold point tropopause (CPT) temperatures based on (a,c,e,g) MERRA-2 and (b,d,f,h) JRA-3Q regressed into (a)–(b) the PC1 trend component (Fig. 3b), (c)–(d) the PC1 interannual variability component (Fig. 3c), (e)–(f) PC2 (Fig. 3d), and (g)–(h) PC3 (Fig. 3e) from Aura MLS (see main text for details). The location of the Tibetan Plateau is marked by a dark grey contour in all panels. Stippling indicates that regressions are significant at the 95% confidence level. The figure corresponds to distributions of cold point temperature anomalies in Figures 6,14 of the main text.
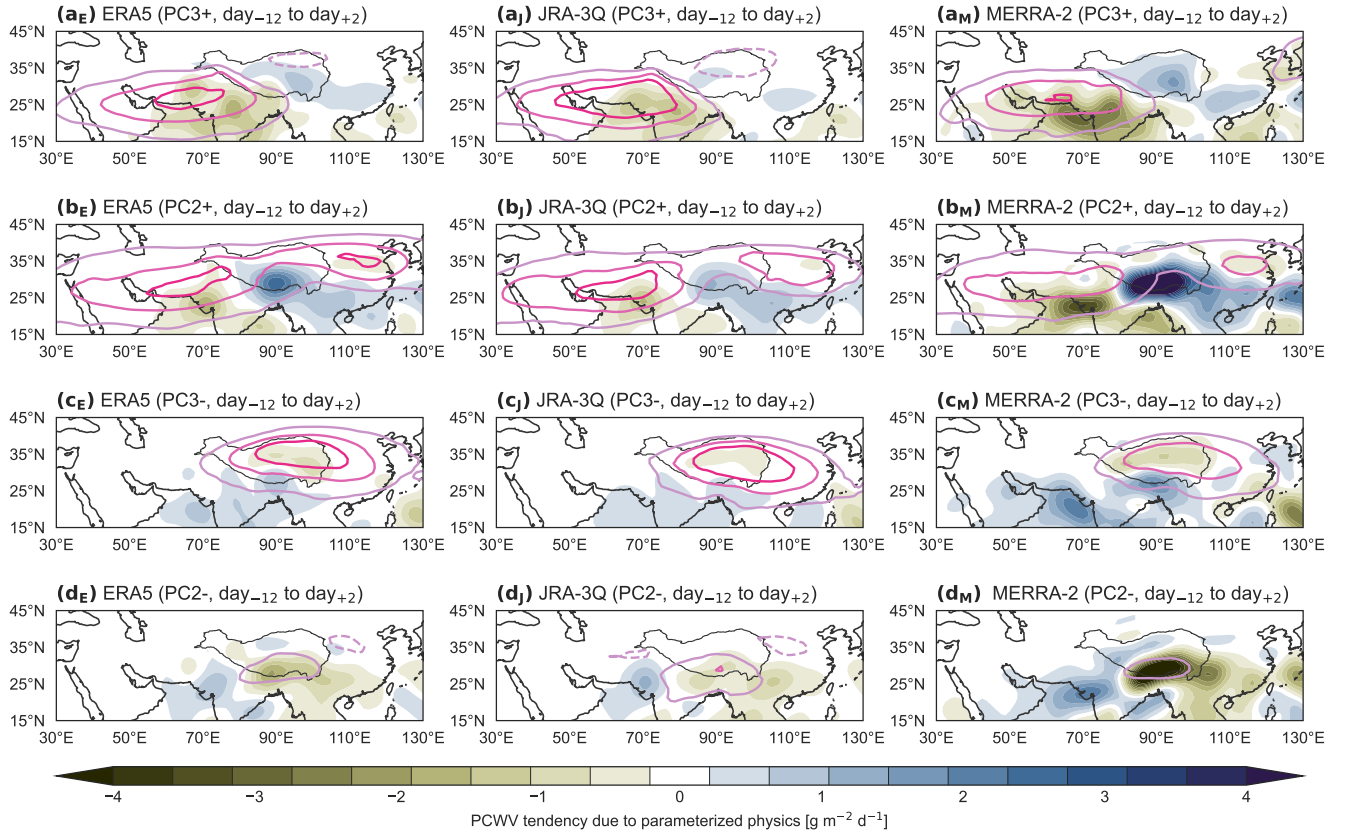
Figure S15. Vertical and horizontal structure of fractional changes in deseasonalized ozone anomalies regressed onto PC3 from Aura MLS (Fig. 3e) based on (a) Aura MLS, (b) JRA-3Q, (c) MERRA-2, (d) M2-SCREAM, (e) ERA5, and (f) CAMS. Fractional anomalies in PCO3 are shown on the top face, meridional mean ozone within 20–25°N along the south face, and zonal mean ozone within 30–130°E along the east face. Dark grey contours mark the location of the Tibetan Plateau and white lines mark the boundaries of the east–west transect in all panels. Stippling indicates where PCO3 regressions are significant at the 95% confidence level. The figure corresponds to Figure 12c in the main text.
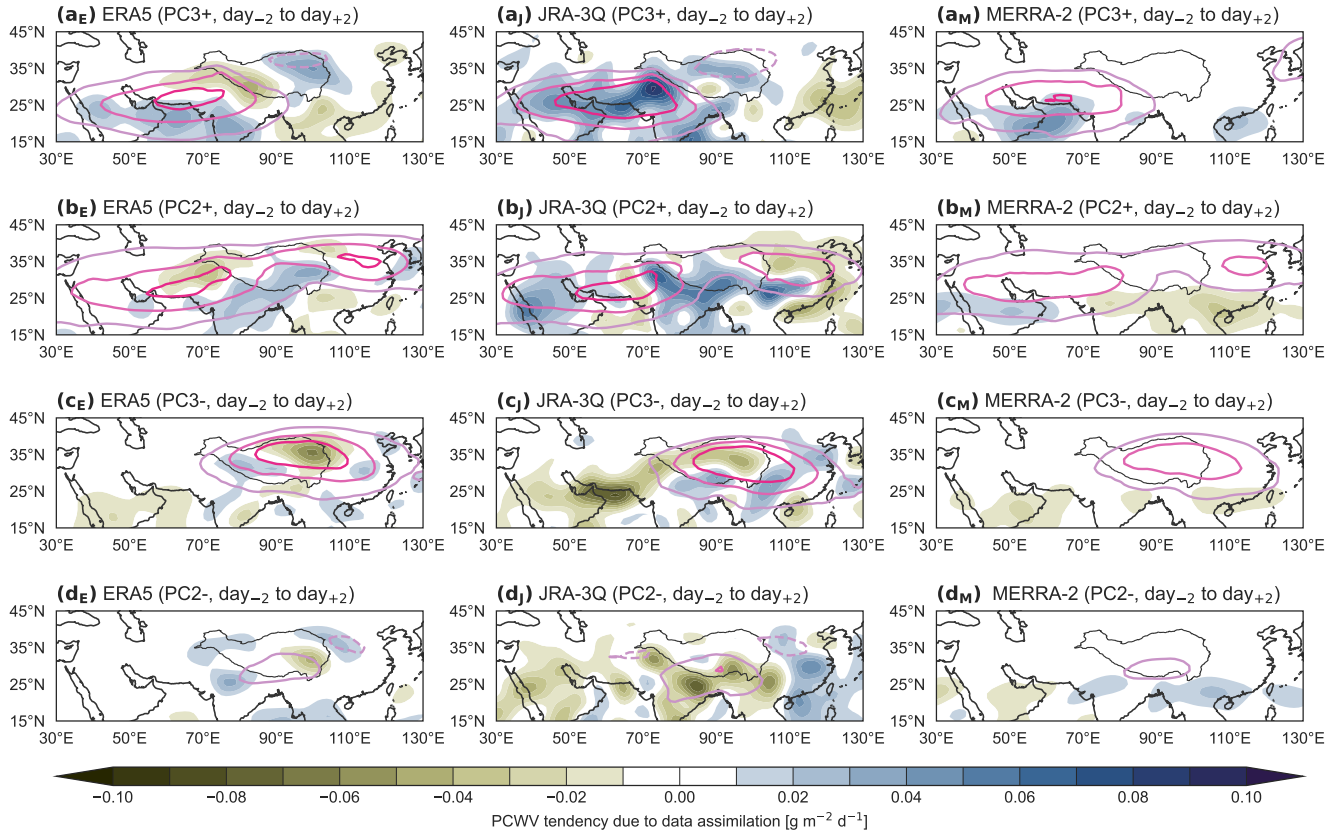
Figure S16. Deseasonalized anomalies regressed onto the third principal component (PC3) of water vapor variability in the monsoon tropopause layer based on Aura MLS (Fig. 3e): (a) radiative heating on the 390 K isentropic surface (shading) and high cloud cover (purple contours; top face), and temperature (shading) and cloud ice water content (purple contours; side faces) based on ERA5; (b) Montgomery streamfunction on the 395 K isentropic surface (top face) and geopotential height (shading; side faces) based on ERA5; (c) outgoing longwave radiation (top face; sign reversed) and non-radiative heating (side faces) based on ERA5. (d,e,f) As in (a,b,c) but for MERRA-2. (g,h,i) As in (a,b,c) but for JRA-3Q. Black contours in (b,e,h) indicate anomalies in the meridional (south face) and zonal (east face) wind. The location of the Tibetan Plateau is marked by a dark grey contour and the boundaries of the east–west transect are marked by white lines in all panels. Stippling on the top face indicates locations where regressions are significant at the 95% confidence level.

Figure S17. Anomalous water vapor tendencies due to dynamics (i.e. moisture flux convergence) for (a_E–d_E) ERA5, (a_J–d_J) JRA-3Q, and (a_M–d_M) MERRA-2 during the 15 days ending on episodes of (a) positive PC3 > 1 (PC3+), (b) positive PC2 > 1 (PC2+), (c) negative PC3 < −1 (PC3−), and (d) negative PC2 < −1 (PC2−). Anomalies in partial column water vapor are marked with pink contours at intervals of 10% from ±10% (negative dashed) during each phase. The location of the Tibetan Plateau is marked by a dark grey contour in all panels.

Figure S18. Anomalous water vapor tendencies due to parameterized physics for (a$_E$–d$_E$) ERA5, (a$_J$–d$_J$) JRA-3Q, and (a$_M$–d$_M$) MERRA-2 during the 15 days ending on episodes of (a) positive PC3 > 1 (PC3+), (b) positive PC2 > 1 (PC2+), (c) negative PC3 < −1 (PC3−), and (d) negative PC2 < −1 (PC2−). Anomalies in partial column water vapor are marked with pink contours at intervals of 10% from ±10% (negative dashed) during each phase. The location of the Tibetan Plateau is marked by a dark grey contour in all panels.

Figure S19. Anomalous water vapor tendencies due to data assimilation for (a_E–d_E) ERA5, (a_J–d_J) JRA-3Q, and (a_M–d_M) MERRA-2 during the 15 days ending on episodes of (a) positive PC3 > 1 (PC3+), (b) positive PC2 > 1 (PC2+), (c) negative PC3 < −1 (PC3−), and (d) negative PC2 < −1 (PC2−). Anomalies in partial column water vapor are marked with pink contours at intervals of 10% from ±10% (negative dashed) during each phase. The location of the Tibetan Plateau is marked by a dark grey contour in all panels. The MERRA-2 assimilation term includes the stratospheric nudging tendency.